Int. J. Multiphase Flow Vol. 16, No. 5, pp. 867–884, 1990
Printed in Great Britain

0301-9322/90 $3.00 + 0.00
Pergamon Press/Elsevier

FILM THICKNESS PREDICTION IN A HORIZONTAL ANNULAR TWO-PHASE FLOW

C. P. Tso[1] and S. Sugawara[2]

[1]Department of Mechanical Engineering, University of Malaya, 59100 Kuala Lumpur, Malaysia

[2]Reactor Engineering Section, O-arai Engineering Center, Power Reactor and Nuclear Fuel Development Corp., O-arai, Japan

(*Received* 18 *May* 1988; *in revised form* 1 *April* 1990)

Abstract—Prediction of developing and transient characteristics of the liquid film in a horizontal annular two-phase flow is carried out using a computer code that provides a three-field representation in subchannel flow. The fully developed steady-state results for film thickness compare satisfactorily with a reported air–water experiment in a pipe 3.9 m long and 32 mm dia. It is concluded that horizontal annular flow modelling may be tractable by the direct application of the conservation equations to mesh cells along the flow.

Key Words: two-phase flow, three-field model, horizontal flow, annular flow, subchannel analysis, liquid film, entrainment, deposition

1. INTRODUCTION

The study of annular liquid–vapour flow is of great importance in thermal engineering, not only because of the need to understand the heat transfer characteristics of such a flow, but also because annular flow may be precursory to liquid dryout in the channel, which is significant in nuclear reactor safety and in corrosion prevention, for instance. However, theoretical modelling of annular two-phase flow is generally more successful in vertical than in horizontal flow. In horizontal flow gravitational force breaks the axial symmetry, resulting in a thicker liquid film at the pipe bottom than at the top. That a liquid film can be sustained at all at the top is of considerable interest, and it provides a qualitative test for the validity of any theoretical model.

Many experimental investigations have been conducted for the water–air pipe system under steady-state, fully developed and adiabatic conditions. One of the earliest experimental studies was by McManus (1961) on the circumferential water film thickness. Later, Anderson & Russell (1970) measured the deposition flux of water droplets in the upper part of the pipe. Butterworth (1972, 1973) made measurements on film thickness as well as axial flowrate. More recently, Fisher & Pearce (1979) measured flowrate, while Laurinat (1978) and Lin *et al.* (1985) made film thickness measurements.

In theoretical development, early analyses were based on condensation models such as those by Chaddock (1957) and Chato (1962), where the upper film was modelled solely by the circumferential flow of the condensate. The mass balance model of Butterworth (1973; Butterworth & Pulling 1973) attempted to account for circumferential and axial flow in the whole pipe by considering the effects of entrainment and deposition. Better entrainment modelling was proposed by Hutchinson *et al.* (1974) and James & Burns (1979), while Wilkes *et al.* (1980) improved on the deposition modelling. Recently, Laurinat *et al.* (1985) considered a formulation that also included an additional stress balance on the film, which gave rise to a recirculating secondary flow. This model was also tested by Lin *et al.* (1985), and was reported to give better results. James *et al.* (1987) proposed further refinement by theorizing on a variable deposition flux. However, none of the models to date give completely satisfactory agreement with the experiments.

The present study attempts a different approach, by applying the full mass and momentum macroscopic conservation equations to the three fluids in a pipe, namely, liquid film, liquid droplets and vapour. This approach has the advantage of predicting not just the steady-state condition, but also the developing annular profile along the pipe, as well as the transient characteristics of the liquid film. The magnitude of the problem requires the use of a computer code, and here the

FIDAS-3DT code (1987) is used. The equations are solved by the finite difference method over divided cells in the channel.

The analysis is carried out to simulate the experimental conditions used in the work of Butterworth & Pulling (1973). Results for liquid water film volume fraction variations around the circumference, through the channel and as a function of time, are presented. The fully developed steady-state results are then compared with the experimental results.

2. THEORY

First the code used in the analysis is described briefly. The "Film Dryout Analysis Code in Subchannels for Three Dimensional Transient Analysis" or FIDAS-3DT code (1987) is a new code developed by the Power Reactor & Nuclear Fuel Development Corp. with the main objective of predicting the dryout and post-dryout heat transfer in rod bundles and the thermal-hydraulic response of nuclear reactor core coolant to loss-of-coolant and power excursion accidents. The code provides a three-field representation (liquid, gas and droplets) of transient two-phase flow in a channel or rod bundle by formulating 12 basic scalar field equations, consisting of 3 continuity equations, 6 momentum equations and 3 energy equations. The capability of the code compares favourably with other existing codes, such as the THERMIT-2 code (Kelly *et al.* 1981) which provides a two-field representation of liquid and vapour by formulating 10 field equations, consisting of 2 continuity equations, 6 momentum equations and 2 energy equations; or the COBRA-TF code (Thurgood *et al.* 1983) which also provides three-field representation by formulating 14 field equations, consisting of 3 continuity equations, 9 momentum equations and 2 energy equations. In addition, FIDAS-3DT provides for entrainment and deposition of droplets, as well as a mechanistic channel dryout prediction (as against an empirical prediction). The HANA code from AERE (U.K.) also provides these features, but it is for steady-state one-dimensional subchannel analysis only.

In the FIDAS-3DT code, by careful division of the flow channel into suitable subchannels, the flow velocity in a subchannel is modelled to have two components: an axial component u, as well as a lateral component v acting on an axial plane, and which is linked to adjacent subchannels. In this way the three-dimensional flow effect is taken into account without the use of a three-component velocity model. The 12 field equations together with the volume fraction conservation relation enable solution for the following 13 parameters: the 6 velocities, the 3 volume fractions, the 3 specific enthalpies and the pressure.

The three-fluid model in the present analysis is depicted in figure 1, where a continuous liquid film surrounds a core of continuous gas which contains suspended entrained liquid droplets. It is assumed that the flow is under adiabatic and isothermal conditions, and there is mass transfer only between the liquid film and droplets by way of entrainment and deposition—as indicated in the figure. The upper part of figure 2 shows the expected water film profile when a steady stream of a uniformly thick water film is injected onto the inner wall of a horizontal pipe. The lower part of figure 2 shows the cell or control volume division. By symmetry only one vertical half is considered, and it is divided into equal lateral (circumferential) sectors as subchannels running throughout the pipe. Each subchannel is further divided into equal axial elements as shown. The complete set of field equations is presented in the appendix.

The field or conservation equations need to be supported by the pertinent hydrodynamic constitutive relations for closure of solution, and generally these relations are still poorly understood in multiphase flow. In this study, simple expressions will be used, as provided by the code, with no major distinction being made between horizontal and vertical flow apart from the difference in the gravitational force terms in the equations.

Firstly, consider droplet entrainment and deposition rates. A number of experiments and correlations have been reported and they were reviewed by Hewitt & Hall Taylor (1970), Ueda (1981), Kataoka & Ishii (1982) and others. Specific modelling for application to horizontal flow was also mentioned in the introduction. For droplet entrainment rate, Hutchinson & Whalley (1972) correlated their data as a function of a dimensionless group given by the product of the interfacial shear stress and the film thickness divided by the surface tension, based on the force balance at the wavy interface between the liquid film and vapour. Ueda (1981) also presented a

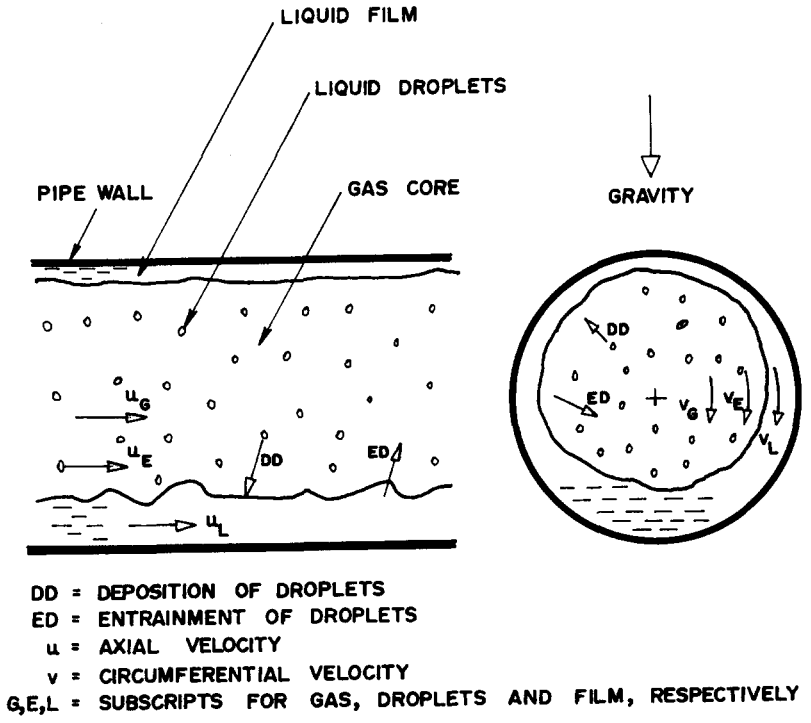

Figure 1. Three-fluid model in horizontal annular flow.

correlation similar to that of Hutchinson & Whalley, and Ueda's correlation is used in the present code. Kataoka & Ishii (1982) proposed a more complicated correlation on the basis of entrainment inception criteria and force balance at the wavy interface. Ueda's model

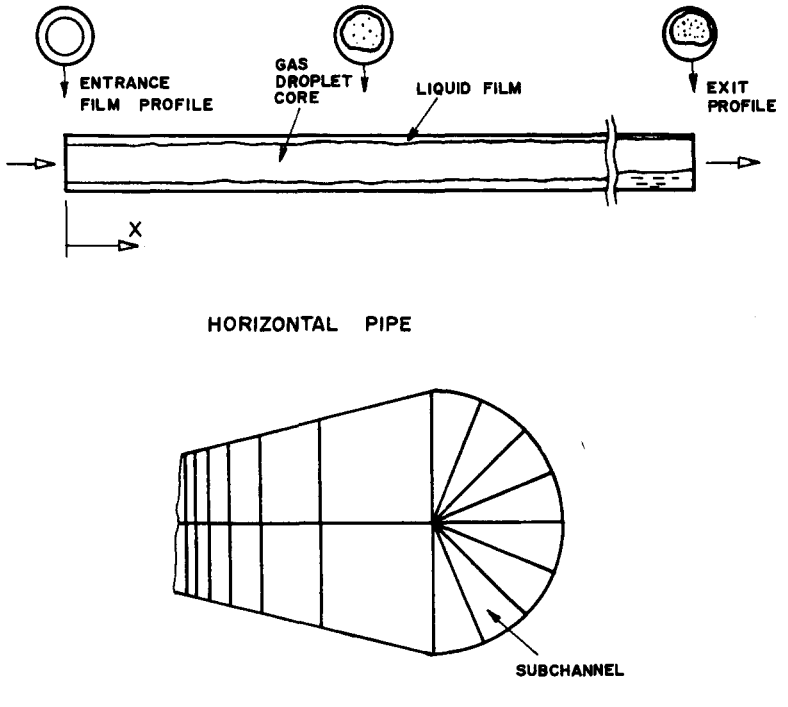

Figure 2. Pipe and cell division.

is based on his experimental air–water and air–alcohol results, where the entrainment rate (in $kg/m^2 s$) is

$$m_E = 3.54 \times 10^{-3} U^{0.57}, \quad \text{when } U > 120, \tag{1}$$

where

$$U = \frac{|\tau_{LG}|}{\sigma}\left(\frac{\epsilon_L u_L}{\sigma}\right)0.6, \tag{2}$$

in which

σ = the air–water surface tension (N/m),
τ_{LG} = the air–water shear stress (N/m^2),
ϵ_L = the volume fraction of the liquid

and

u_L = the velocity of the liquid (m/s).

The deposition of droplets is usually expressed by a deposition coefficient. Paleev & Filippovich (1966) derived a correlation from their experimental data in atmospheric air–water flow which gave the deposition coefficient as a function of gas velocity, gas Reynolds number and the ratio of droplet density to gas density. Whalley (1977) recommended a coefficient in terms of the surface tension, while Bennett *et al.* (1966) and Saito *et al.* (1978) correlated the coefficient as a function of droplet concentration. Recently, Sugawara (1988) proposed a model based on the turbulent diffusivity of entrained droplets in the vapour core. In the present study, the simple model by Farmer *et al.* (1970) is used. In their model, the deposition rate is given by

$$m_D = k_f C, \tag{3}$$

where k_f (in m/s) and C (in kg/m^3) are the droplet transfer coefficient and average droplet density, respectively, and are given by

$$k_f = \tfrac{1}{4}\lambda D u_G \tag{4}$$

and

$$C = \frac{\epsilon_E \rho_E}{(\epsilon_E + \epsilon_G)}. \tag{5}$$

In the above,

λ = a constant dependent on the droplet diameter (m^{-1}),
D = the pipe inner diameter (m),
u_G = the gas velocity (m/s),
ϵ_E, ϵ_G = the volume fraction of droplets and gas, respectively

and

ρ_E = the density of the droplets (kg/m^3).

Turning now to the interfacial resistances, the wall–liquid drag force (in N/m^3) is based on Blasius' form, as illustrated by the following:

$$\bar{\tau}_{WL} = \bar{A}_{WL} K_{WL} \frac{\rho_L}{2} u_L |u_L|, \tag{6}$$

where ρ_L is the liquid density, $\bar{A}_{WL}$ is the wall–liquid average area (in m^{-1}), given by

$$\bar{A}_{WL} = \frac{4}{D}, \tag{7}$$

the Blasius expression (dimensionless) is given by

$$K_{WL} = \frac{1}{4}\left(\frac{0.316}{Re_L^{0.25}}\right) \tag{8}$$

and the liquid film Reynolds number is

$$\mathrm{Re}_L = \frac{u_L D}{\nu_L}, \quad [9]$$

in which ν_L is the kinetic viscosity of the liquid film.

In the case of the vapour–liquid drag force, the code uses Ueda's (1981) model, although other models exist in the literature, including the wave velocity model and the Wallis model (Wallis 1969). Ueda (1981) advocates the expression

$$\bar{\tau}_{LG} = \bar{A}_{LG} K_{LG} \frac{\rho_G}{2} (u_G - u_L)|u_G - u_L|, \quad [10]$$

where the vapour–liquid interfacial average area (in m^{-1}) is

$$\bar{A}_{LG} = \left(\frac{4}{D}\right)(1 - \epsilon_L)^{1/2} \quad [11]$$

and

$$K_{LG} = \frac{1}{4} \times (2.85 - 2.10\epsilon_G^{2.20})^4 \left[\frac{(\rho_L - \rho_G) g D_{LG}}{\rho_G (u_G - u_L)^2}\right]^{0.7} \times \left[\frac{\mu_G |u_G - u_L|}{\mu_L u_L}\right]^{0.1} \left[\frac{|u_G - u_L| D_{LG}}{\nu_G}\right]^{-0.2} \times C_H, \quad [12]$$

D_{LG} is the diameter of the vapour–droplet flow section and C_H is a correction factor for horizontal flow, taken to be 2.

For the vapour–droplet drag force the conventional single-phase correlation is used. Thus,

$$\bar{\tau}_{EG} = \bar{A}_{EG} K_{EG} \frac{\rho_G}{2} (u_G - u_E)|u_G - u_E|, \quad [13]$$

where the vapour–droplet area (total cross-sectional droplet area) is

$$\bar{A}_{EG} = \frac{3\epsilon_E}{2\delta_D} \quad [14]$$

and the coefficient K_{EG} is taken to be (Morōka *et al.* 1984)

$$K_{EG} = \frac{24}{\mathrm{Re}_\delta}(1 + 0.15\mathrm{Re}_\delta^{0.687}) + \frac{0.42}{1 + 4.25 \times 10^4 \mathrm{Re}_\delta^{-1.16}}, \quad [15]$$

where δ_D is the droplet diameter and

$$\mathrm{Re}_\delta = \frac{|u_G - u_E| \delta_D}{\nu_E}. \quad [16]$$

in the code, the average droplet size is determined by

$$\delta_D = \begin{cases} \dfrac{\sigma \mathrm{We}}{\rho_G (u_G - u_E)^2} \\ 10^{-3}, \qquad \text{if } \delta_D < 10^{-3}, \end{cases} \quad [17]$$

where We is the Weber number.

Lastly, in turbulent momentum and mass diffusion modelling, the generalized Prandtl mixing length theory is used in the following expressions for molecular and turbulent viscous stresses:

$$\tau_{GxX} = -2(\mu_G + \mu_G^T)\frac{\partial u_G}{\partial L} + 3\rho_G l_m^2 \sum_k \left(\frac{\partial u_G}{\partial L} + \frac{\partial v_G}{\partial x}\right)_k^2, \quad [18]$$

$$\tau_{GLx} = -(\mu_G + \mu_G^T)\left(\frac{\partial u_G}{\partial L} + \frac{\partial v_G}{\partial x}\right) \quad [19]$$

and

$$\tau_{GLL} = -2(u_G + \mu_G^T)\frac{\partial v_G}{\partial L} + 3\rho_G l_m^2 \sum_k \left(\frac{\partial v_G}{\partial L} + \frac{\partial v_G}{\partial x}\right)_k^2, \quad [20]$$

where μ_G is the dynamic viscosity of the gas, μ_G^T is the turbulent dynamic viscosity of the gas, given by

$$\mu_G^T = \rho_G l_m^2 \left[\sum_k \left(\frac{\partial u_G}{\partial L} + \frac{\partial v_G}{\partial x} \right)_k^2 \right]^{1/2}, \quad [21]$$

and l_m is the momentum mixing length, taken as the equivalent diameter. Equations [18]–[20] are pertinent in the field equations [A.7] and [A.8]. Similarly, the following terms appear in [A.11] and [A.12]:

$$\tau_{Lxx} = -2(\mu_L + \mu_L^T) \frac{\partial u_L}{\partial x} + 3\rho_L l_m^2 \sum_k \left(\frac{\partial u_L}{\partial L} + \frac{\partial v_L}{\partial x} \right)_k^2, \quad [22]$$

$$\tau_{LLx} = -(\mu_L + \mu_L^T) \left(\frac{\partial u_L}{\partial L} + \frac{\partial v_L}{\partial x} \right) \quad [23]$$

and

$$\tau_{LLL} = -2(\mu_L + \mu_L^T) \frac{\partial v_L}{\partial L} + 3\rho_L l_m^2 \sum_k \left(\frac{\partial u_L}{\partial L} + \frac{\partial v_L}{\partial x} \right)_k^2. \quad [24]$$

3. PRESENT STUDY

In the present study, the fluids are water and air, the three fields being the continuous water film, the continuous air and the entrained water droplets suspended in the air. In accordance with the AERE experimental conditions (Butterworth & Pulling 1973), two sets of flow conditions are simulated which are referred to as high water flow (or high flow) and low water flow (or low flow), respectively. Details are given in table 1.

According to the two-phase flow pattern map by Scott (1963), both sets of flow conditions are expected to exhibit dispersed annular flow characteristics.

Referring to the lower part of figure 2 again, in the present formulation, there are 8 lateral sectors and 39 equal axial parts. The complete mesh structure is shown in figure 3, where the physical parameters are associated with either a node, corresponding to the centre of a cell, or a junction, corresponding to a cell boundary. Thus, laterally there are 8 L-nodes ($j = 1$ to 8) and 7 L-junctions ($k = 1$ to 7). Axially, in order to specify parameters at both ends of the pipe, 2 imaginary cells are created, giving rise to 41 x-nodes (at $x = \frac{1}{2}, 1\frac{1}{2}, \ldots, 40\frac{1}{2}$) and 42 x-junctions (at $x = 0, 1, \ldots, 41$). Figure 4 shows a unit cell, indicating the subscript notation as well as the fact that velocities are specified at a junction, and volume fractions, specific enthalpies and pressure are specified at the node. Fluid properties such as densities, which are all specified at a node, are calculated by the code's library file, and at a junction an average value of those at adjacent nodes is calculated.

The specifications for the inlet conditions are the inlet velocities and the inlet volume fractions of water, air and droplets; the enthalpies and densities of water and air being at 300 K. The initial condition at the pipe outlet is the exit pressure of 2.5 bar. All heat transfer mechanisms are neglected.

The inlet velocities and volume fractions are obtained based on (a) the experimental inlet flow rates of water, air and droplets, the droplet flowrate being zero, and (b) the average experimental film thickness, taken to be distributed uniformly at the inlet. It is noteworthy that the outlet film

Table 1. Flow conditions in the horizontal pipe

Pipe length (m)	3.9	
Pipe internal dia (mm)	32.0	
Ambient temperature (K)	300.0	
Test section pressure (bar)	2.5	
	Entrance conditions	
	High flow	Low flow
Water flowrate (kg/s)	0.128	0.064
Air flowrate (kg/s)	0.025	0.051

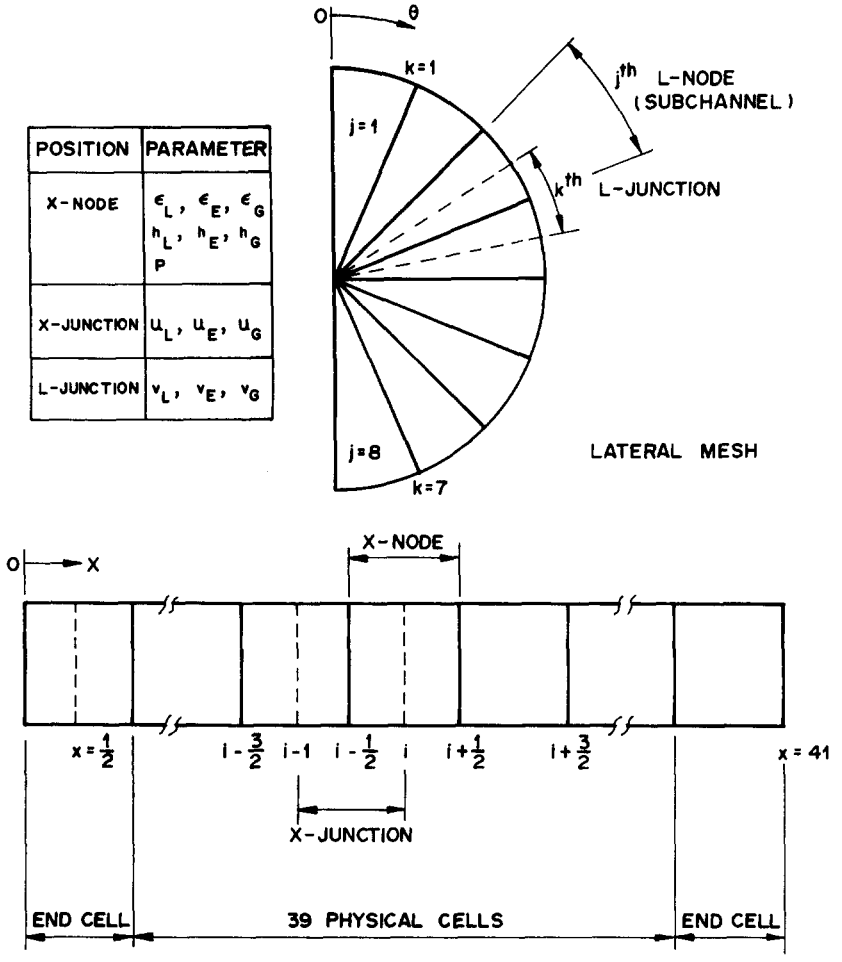

Figure 3. Mesh structure.

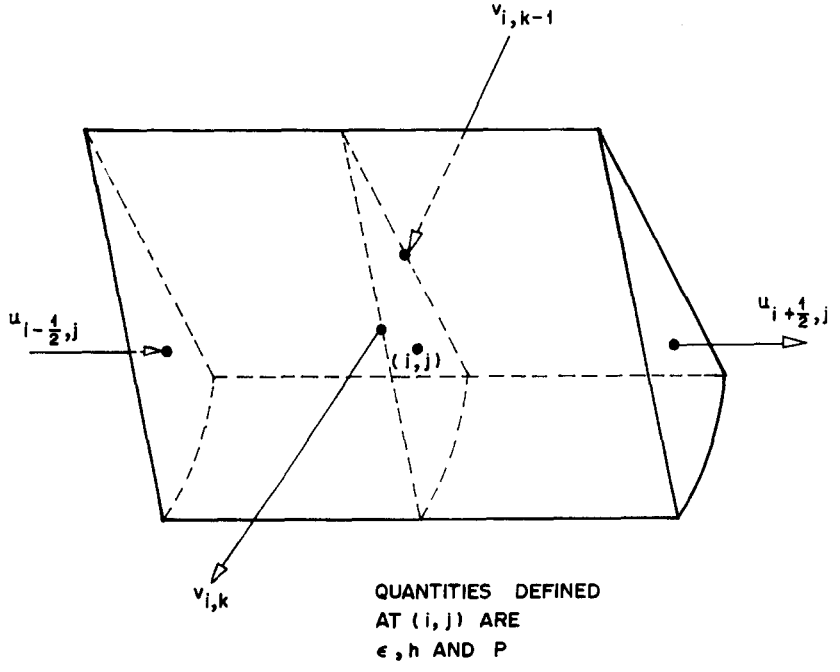

Figure 4. A unit mesh cell.

thickness distribution in the present study is obtained by using the time marching method. That is, steady state is obtained as an asymptotic solution of the transient simulation under constant boundary conditions. Parametric study on the outlet film thickness distribution has shown that the predicted values are insensitive to the initial condition of the film thickness distribution at the inlet, since the test section used in the experiment of Butterworth & Pulling (1973) is long enough to obtain the equilibrium condition at the outlet.

The finite difference equations obtained are linearized by means of Taylor's expansion, and the linear finite difference matrix equations are solved using the Skyline solver. The solution logic involves solving first for pressure, next for the products of volume fraction with velocity or specific enthalpy, then for each volume fraction and, finally, the individual velocities and specific enthalpies. The computational scheme is based on a semi-implicit method similar to the RELAPS algorithm (Ransom *et al.* 1981). The Fujitsu FACOM-M-380 machine is used in the present study.

To ensure stability, each time-step is automatically controlled by taking a value in accordance with the rule that one-tenth of the smallest time-step is selected from 12 values calculated in the following ways: firstly, from the Courant condition, 6 values are calculated corresponding to the three-fluid velocities for axial and circumferential directions; secondly, from viscous diffusion consideration, 2 values corresponding to air and water are calculated; and similarly, 4 more values are calculated from thermal diffusion and mass diffusion considerations, respectively.

4. RESULTS

The average CPU time per time-step in the computation is about 0.64 s. For the high water flow runs, a total of 79,325 time-steps are taken to reach a physical time of 3.00 s, the last time-step being 0.0000744 s. For the low water flow runs, a total of 108,000 time-steps are taken to compute a physical time of 2.92 s, with the last time-step being 0.0000425 s. Thus, a total of CPU time of about 30 h are consumed in the present study.

The graphical results for the high water flow case only are shown in figures 5 and 6. Figures 5(a–f) show the time-dependent graphs in 3 subchannels at the downstream position (x-node 40 or x-junction 41) for volume fractions, film velocity, pressure and film specific enthalpy. Figures 6(a–f) show the results for the steady, developing flow along the pipe in 3 subchannels for volume fractions, film velocity, pressure and gas velocity. From the results for film volume fractions in each subchannel, the water film thicknesses δ may be calculated from the relation

$$\delta = \tfrac{1}{2}D[1 - (1 - \epsilon_L)^{1/2}], \qquad [25]$$

where D is the pipe diameter. This is based on the assumption of annular flow with all the water being present at the wall of the subchannel.The final results are tabulated in table 2 and plotted in figures 7 and 8.

5. DISCUSSION

Referring to figure 5(a), the film volume fraction ϵ_L at position x-node 40 is as expected—greatest in the lowest subchannel (No. 8) and least in subchannel 1. In the first 0.1 s, ϵ_L is increasing in subchannel 8, while decreasing in subchannels 4 and 1. Henceforth over the next 1.5 s the values decrease to steady-state values, as those given in table 2. For the gas volume fraction ϵ_G the trend is reversed, as shown in figure 5(b). This is in conformation with [A.14], since the droplet volume fraction ϵ_E is small, as indicated in figure 5(c). The actual values for ϵ_E at steady state are 5×10^{-5}, 9.43×10^{-5} and 4.48×10^{-5} for subchannels 1, 4 and 8, respectively. The axial film velocity u_L is shown in figure 5(d). The pressure shown in figure 5(e) indicates a region of instability during the first 0.1 s or so, before decreasing to state steady at 1.5 s. The film specific enthalpy in figure 5(f) displays a constant value, meeting the isothermal adiabatic conditions of the problem.

Turning to the developing flow characteristics along the pipe in figures 6(a–f) it is seen from figures 6(a–c) that the volume fractions in each subchannel attain their fully developed values by the time the mid-section of the pipe is reached, with the greatest changes occurring within the first 0.5 m. The gravitational effects are clearly manifested by the bottom subchannel (No. 8) increasing,

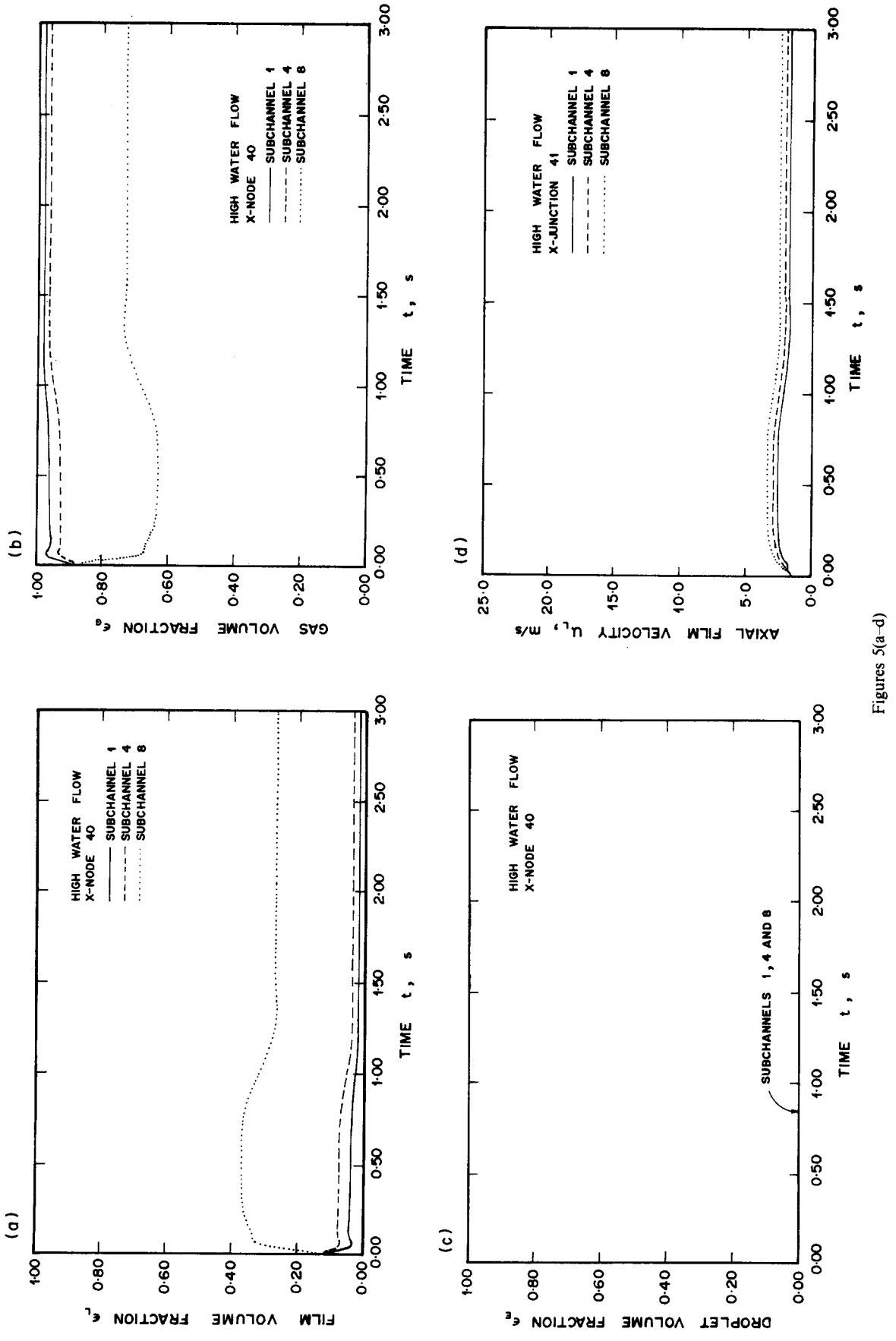
(a)
FILM VOLUME FRACTION ϵ_L
HIGH WATER FLOW
X-NODE 40
SUBCHANNEL 1
SUBCHANNEL 4
SUBCHANNEL 8
TIME t, s
(b)
GAS VOLUME FRACTION ϵ_g
HIGH WATER FLOW
X-NODE 40
SUBCHANNEL 1
SUBCHANNEL 4
SUBCHANNEL 8
TIME t, s
(c)
DROPLET VOLUME FRACTION ϵ_e
HIGH WATER FLOW
X-NODE 40
SUBCHANNELS 1, 4 AND 8
TIME t, s
(d)
AXIAL FILM VELOCITY u_L, m/s
HIGH WATER FLOW
X-JUNCTION 41
SUBCHANNEL 1
SUBCHANNEL 4
SUBCHANNEL 8
TIME t, s

Figures 5(a–d)

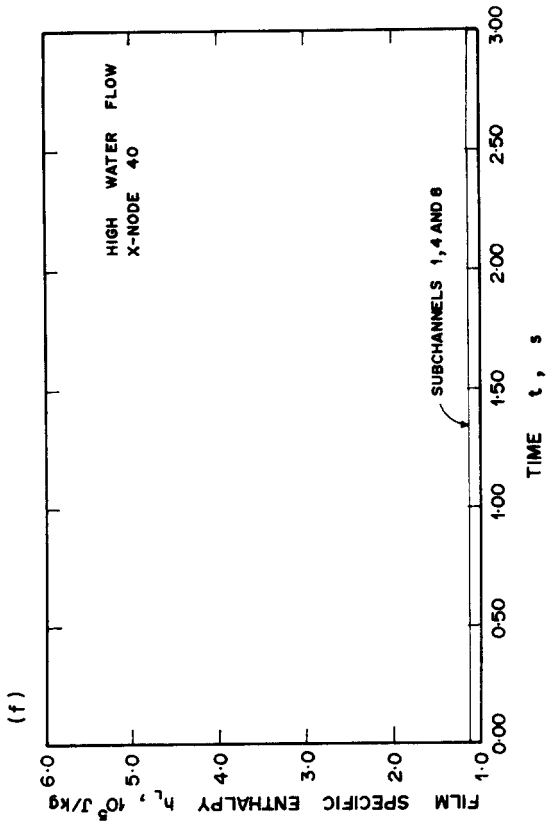

Figures 5(e,f)

Figures 5(a–f). Results for time-dependent flow downstream.

Figures 6(a,b)

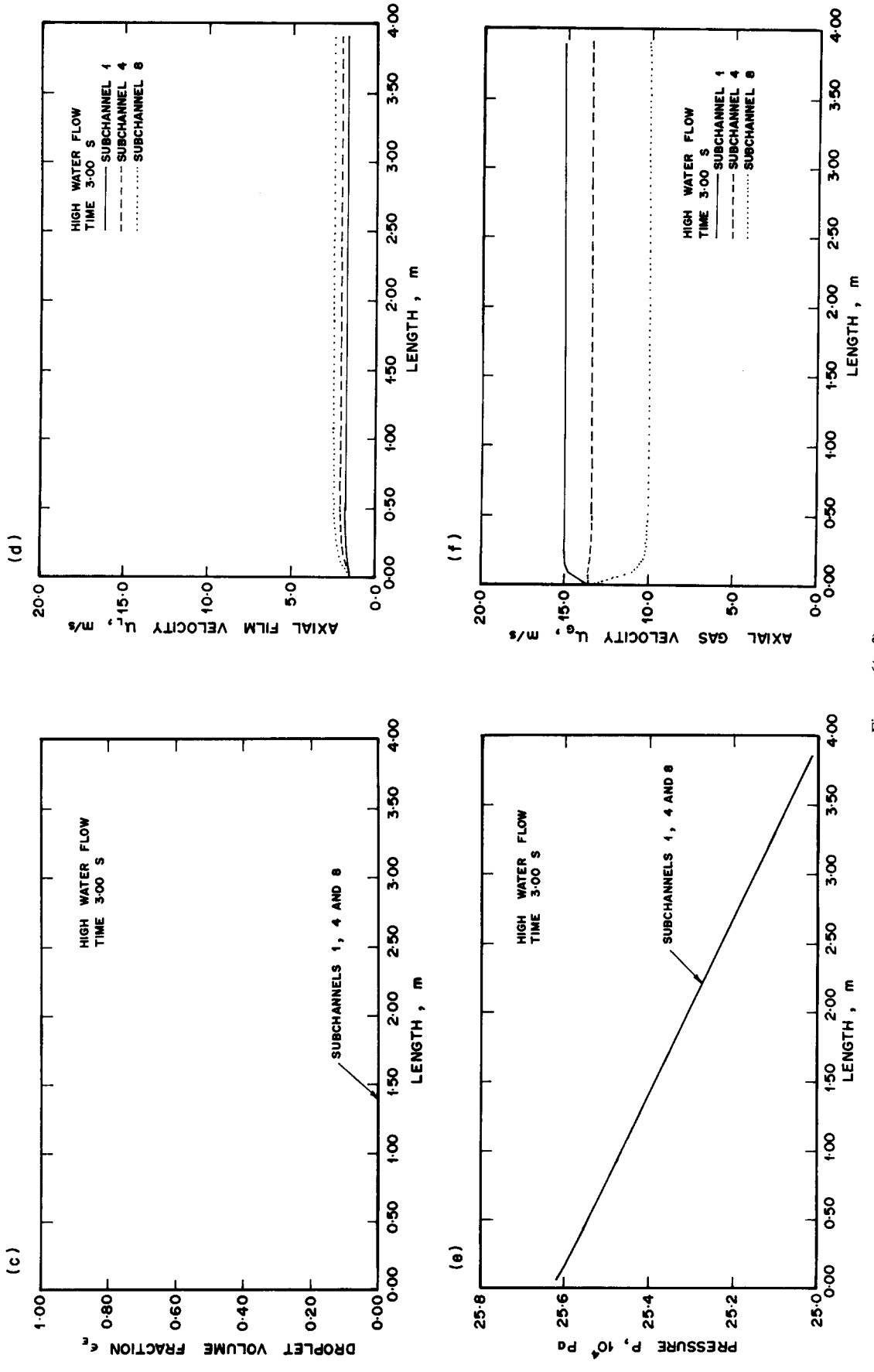

Figures 6(a–f). Results for steady, developing flow along the pipe.

Table 2. Water film thicknesses

Subchannel No.	Angular position, θ (deg)	High flow case		Low flow case	
		Void fraction, ϵ_L	Film thickness, δ (mm)	Void fraction, ϵ_L	Film thickness, δ (mm)
1	11.25	0.0187	0.150	0.0157	0.126
2	33.75	0.0224	0.180	0.0184	0.148
3	56.25	0.0241	0.194	0.0194	0.156
4	78.75	0.0370	0.299	0.0290	0.234
5	101.25	0.0394	0.318	0.0303	0.245
6	123.75	0.0798	0.651	0.0617	0.502
7	146.25	0.0832	0.680	0.0629	0.511
8	168.75	0.270	2.33	0.131	1.08

while subchannels 1 and 4 are decreasing, in film thickness. Also shown in figures 6(d–f) are the film and gas velocities, as well as the linear pressure drop in the pipe. As expected, the bulk water flow in the bottom subchannel (No. 8) has a slightly higher velocity than the other subchannels, while the gas flow is highest in the top subchannel (No. 1) where the gas–water interfacial interference is probably the lowest.

With respect to the steady fully developed water film thickness, table 2 shows that there is a variation of about 16 fold between the thinnest film in subchannel 1, of thickness 0.150 mm, and the thickest film in subchannel 8, 2.33 mm. The calculated results are compared with the experimental results in figure 7, showing that the calculated results appear to be quite close to the reported measured mean thicknesses from $\theta = 0°$ to 80°, corresponding to subchannels 1–4. Beyond this, calculated results are lower, to a maximum of about a factor of 3. However, the calculated results lie within the region of the measured wave height and substrate height. The film thicknesses were measured by the needle contact technique (Butterworth & Pulling 1973), with the wave height and substrate height denoting, respectively, the thicknesses for 2 and 98% probability of contact

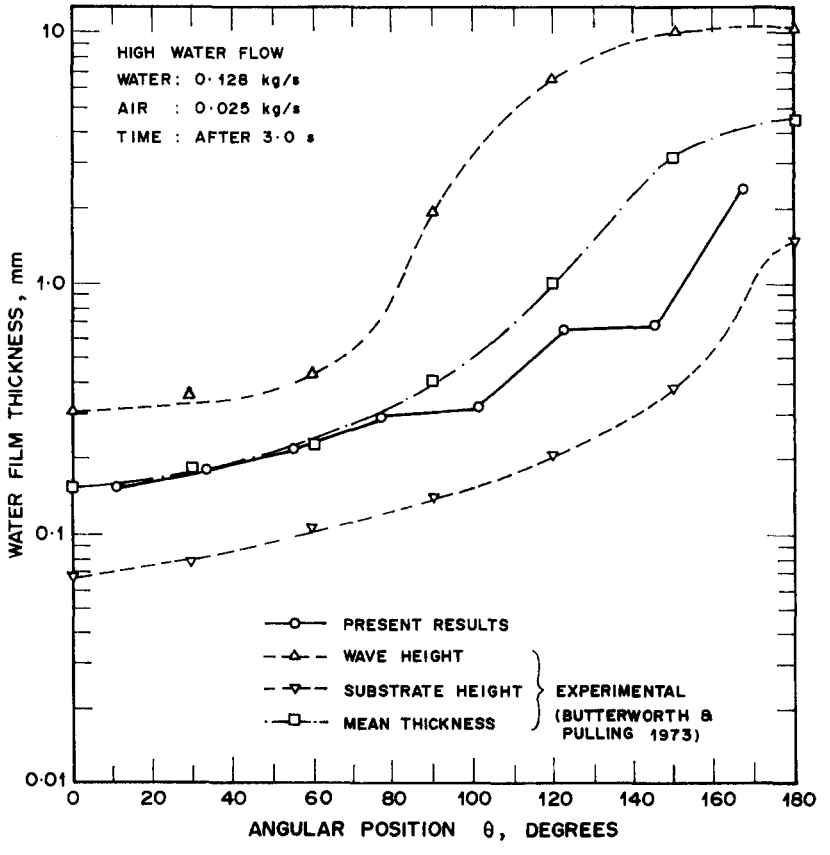

Figure 7. Steady results for film thicknesses in the high water flow case.

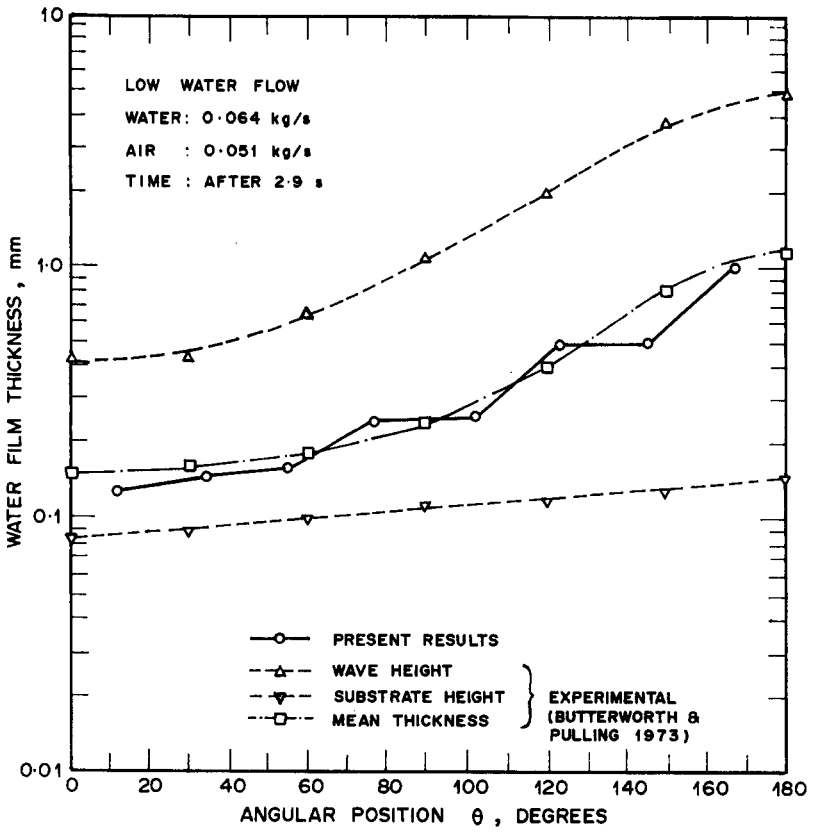

Figure 8. Steady results for film thicknesses in the low water flow case.

with the film, and thus they may be regarded as representing the upper and lower limits of the film thickness.

The corresponding results for the low water flow case are generally similar to those for the high water flow case. Table 2 shows that the variation in film thicknesses is about 9 fold, from 0.126 mm at the top to 1.08 mm at the bottom. Figure 8 shows that the calculated film thicknesses match well with the experimental values.

It is noteworthy that since the experimental results are for steady flow, it is of importance that the calculated results are also for such conditions. Further confidence that steady conditions will prevail beyond the physical time of 3 s is given by a side-study, where runs are made up to a physical time of 10 s for a one-dimensional model without diffusion and mixing effects. The one-dimensional results which consume much less computer time are qualitatively similar to the three-dimensional runs and they show that conditions are indeed steady, from around 2 s onwards.

6. CONCLUDING REMARKS

An analysis of horizontal air–water annular adiabatic flow has been carried out successfully with the FIDAS-3DT code. Under specified input conditions the calculated results give fair agreement with the experimental results for water film thicknesses at steady, fully developed state. Results are also available for the transient and developing states along the pipe, although their validity has yet to be confirmed by experiments. Obviously, the results may be improved by increasing the number of subchannels. However, the accuracy of the present analysis is affected not only by the modelling, but also by how good the constitutive relations are. As pointed out by James *et al.* (1987), the limitations of theoretical modelling may be due to the lack of information on contributing mechanisms in the flow. Until the roles of such mechanisms as entrainment flux, interfacial shear stress and turbulence are better understood in multiphase flow, there will not be complete confidence in theoretical modelling. Nevertheless, in spite of using simple constitutive relations, the present results are encouraging enough to advocate further exploration by using such

an approach for horizontal annular flow analysis. Results for flow rate prediction will be reported elsewhere.

Acknowledgements—The assistance given by K. Watanabe in the present work is gratefully acknowledged. The contribution by one of us (C.P.T.) was made possible through an award by the Japan Science and Technology Agency. The authors thank the reviewers for their constructive criticisms.

REFERENCES

ANDERSON, R. J. & RUSSELL, T. W. F. 1970 Circumferential variation of interchange in horizontal annular two-phase flow. *Ind. Engng Chem. Fundam.* **9,** 340–344.

BENNETT, A. W., HEWITT, G. F., KEARSEY, H. A., KEEYS, R. K. F. & PULLING, D. J. 1966 Studies of burnout in boiling heat transfer to water in round tubes with non-uniform heating. UKAEA Report No. AERE-R5076.

BUTTERWORTH, D. 1972 Air–water annular flow in a horizontal tube. *Prog. Heat Mass Transfer* **6,** 235–251.

BUTTERWORTH, D. 1973 An analysis of film flow for horizontal annular flow and condensation in a horizontal tube. UKAEA Report No. AERE-R7575.

BUTTERWORTH, D. & PULLING, D. J. 1973 Film flow and film thickness measurements for horizontal, annular, air–water flow. UKAEA Report No. AERE-R7576.

CHADDOCK, J. B. 1957 Film condensation of vapour in a horizontal tube. *Refrigng Engng* **Apr.,** 36–41, 90–95.

CHATO, J. C. 1962 Lamina condensation inside horizontal and inclined tubes. *ASHRAE Jl* **Feb.,** 52–60.

COLLIER, J. G. 1972 *Convective Boiling and Condensation.* McGraw-Hill, New York.

FARMER, R., GRIFFITH, P. & ROHSENOW, W. M. 1970 Liquid droplet deposition in two-phase flow. *Trans. ASME Ser. C* **92,** 587–594.

FIDAS-3DT CODE 1987 Internal report, Power Reactor and Nuclear Fuel Corp., O-arai Engineering Center, O-arai, Japan (in Japanese).

FISHER, S. A. & PEARCE, D. L. 1979 A theoretical model for describing horizontal annular flows. In *Two-phase Momentum, Heat and Mass Transfer in Chemical, Process, and Energy Engineering Systems* (Edited by DURST, F., TSIKLAURI, G. V. & AFGAN, N.), pp. 327–337. Hemisphere/McGraw-Hill, Washington, D.C.

HEWITT, G. F. & HALL-TAYLOR, N. S. 1970 *Annular Two-phase Flow.* Pergamon Press, Oxford.

HUTCHINSON, P. & WHALLEY, P. B. 1972 A possible characterization of entrainment in annular flow. UKAEA Report No. AERE-R7126.

HUTCHINSON, P., BUTTERWORTH, D. & OWEN, R. G. 1974 Development of a model for horizontal annular flow. UKAEA Report No. AERE-R7789.

JAMES, P. W. & BURNS, A. 1979 Further developments in the modelling of horizontal annular flow. UKAEA Report No. AERE-R9373.

JAMES, P. W., WILKES, N. S., CONKIE, W. & BURNS, A. 1987 Developments in the modelling of horizontal annular two-phase flow. *Int. J. Multiphase Flow* **13,** 173–198.

KATAOKA, I. & ISHII, M. 1982 Mechanism and correlation of droplet entrainment and deposition in annular two-phase flow. Report ANL-82-44.

KELLY, J. E., KAO, S. P. & KAZIMI, M. S. 1981 THERMIT-2: a two-fluid model for light water reactor subchannel transient analysis. Report No. MIT-EL-81-014.

LAURINAT, J. E. 1978 Studies of the effects of pipe size on horizontal annular two-phase flows. Ph.D. Thesis, Univ. Illinois, Urbana.

LAURINAT, J. E., HANRATTY, T. J. & JEPSON, W. P. 1985 Film thickness distribution for gas–liquid annular flow in a horizontal pipe. *Physicochem. Hydrodynam.* **6,** 179–195.

LIN, T. F., JONES, O. C. JR, LAHEY, R. T. JR, BLOCK, R. C. & MURASE, M. 1985 Film thickness measurements and modelling in horizontal annular flows. *Physicochem. Hydrodynam.* **6,** 197–206.

MCMANUS, H. N. 1961 Local liquid distribution and pressure drops in annular two-phase flow. Presented at *ASME–EIC Hydraulic Conf.*, Montreal, Paper 61-HYD-20.

MORŌKA, S., ISHIZUKA, T. & KAGAWA, T. 1984 Development of POST-MULTI code for the analysis of heat transfer beyond boiling transition. *J. Atom. Energy Soc. Japan* **26,** 136–138 (in Japanese).

PALEEV, I. I. & FILIPPOVICH, B. S. 1966 Phenomena of liquid transfer in two-phase dispersed annular flow. *Int. J. Heat Mass Transfer* **9,** 1089–1093.

RANSOM, V. H., WAGNER, R. J., TRAPP, J. A., CARLSON, K. E., KISER, D. M., KUO, H. H., CHOW, H., NELSON, R. A. & JAMES, S. W. 1981 RELAP5/MOD1 Code Manual. Report NUREG/CR-1926, EG&G Idaho Inc., Idaho Falls.

SAITO, T., HUGHES, E. D. & CARBON, M. W. 1978 Multi-fluid modelling of annular two-phase flow. *Nucl. Engng Des.* **50,** 225–271.

SCOTT, D. S. 1963 Properties of cocurrent gas–liquid flow. *Chem. Engng* **4,** 199–277.

SUGAWARA, S. 1988 Droplet deposition and entrainment modelling based on the three-fluid model. In *Proc. 3rd Int. Top. Meet. on Nuclear Power Plant Thermal Hydraulics and Operations*, Seoul, Korea, Vol. A1, pp. 19–28.

THURGOOD, M. J., CUTA, J. M., KOONTZ, A. S. & KELLY, J. M. 1983 COBRA/TRAC-A thermal hydraulics code for transient analysis of nuclear reactor vessels and primary coolant systems. Report NUREG/CR-3046, Pacific Northwest Lab. Richland, Wash.

UEDA, T. 1981 *Two-phase Flow—Flow and Heat Transfer*. Yokendo, Japan (in Japanese).

WALLIS, G. B. 1969 *One-dimensional Two-phase Flow*. McGraw-Hill, New York.

WHALLEY, P. B. 1977 The calculation of dryout in rod bundles. *Int. J. Multiphase Flow* **3,** 501–515.

WILKES, N. S., CONKIE, W. & JAMES, P. W. 1980 A model for the droplet deposition rate in horizontal annular two-phase flow. UKAEA Report No. AERE-R9691.

APPENDIX

Field Equations

The following field equations for incompressible flow are applied to each fluid in a unit cell. They are written in the general form to include the effect of heat transfer amongst the fluids, as these general forms are actually used in the code for this adiabatic problem. Subscripts G, E and L refer to the gaseous fluid, entrained liquid droplets and liquid film, respectively.

Mass conservation equations

For the gaseous fluid,

$$\frac{\partial}{\partial t}(\epsilon_G \rho_G) = -\frac{1}{A}\frac{\partial}{\partial x}(\epsilon_G \rho_G u_G A) + \frac{1}{A}\sum_k (\epsilon_G \rho_G v_G S_L)_k + (\Gamma_{LG} - \Gamma_{GF} + \dot{m}_{LG}) + (\Gamma_{EG} - \Gamma_{GE} + \dot{m}_{EG}) + \frac{\partial}{\partial x}\left[\epsilon_G (D_{CG} + D_{CG}^T)\frac{\partial \rho_G}{\partial x}\right] - \frac{1}{A}\sum_k \left[S_L \epsilon_G (D_{CG} + D_{CG}^T)\frac{\partial \rho_G}{\partial L}\right]_k, \quad [A.1]$$

where

ϵ_G = volume fraction of the gas,
ρ_G = density of the gas,
A = x-direction cross-sectional area,
u_G = axial velocity of the gas,
v_G = circumferential velocity of the gas,
S_L = side length of the subchannel,
Γ_{LG} = film to gas evaporation rate per unit volume,
Γ_{GL} = gas to film condensation rate per unit volume,
$\dot{m}_{LG}$ = film to gas convective evaporation,
Γ_{EG} = droplets to gas evaporation rate per unit volume,
Γ_{GE} = gas to droplets condensation rate per unit volume,
$\dot{m}_{EG}$ = droplets to gas convective evaporation rate per unit volume,
D_{CG} = diffusion coefficient for the gas,
D_{CG}^T = turbulent diffusion coefficient for the gas,
t = time,

x = axial distance,
L = lateral (circumferential) distance

and

k = index referring to the number of open lateral sides in the subchannel (two in the present problem).

Similarly, for the entrained liquid droplets,

$$\frac{\partial}{\partial t}(\epsilon_E \rho_E) = -\frac{1}{A}\frac{\partial}{\partial x}(\epsilon_E \rho_E u_E A) + \frac{1}{A}\sum_k (\epsilon_E \rho_E v_E S_L)_k + (\Gamma_{GE} - \Gamma_{EG} - \dot{m}_{EG}) - \frac{S}{A}(m_D - m_E) + \frac{\partial}{\partial x}\left[\epsilon_E (D_{CE} + D_{CE}^T)\frac{\partial \rho_E}{\partial x}\right] - \frac{1}{A}\sum_k \left[S_L \epsilon_E (D_{CE} + D_{CE}^T)\frac{\partial \rho_E}{\partial L}\right]_k, \quad [A.2]$$

and for the liquid film,

$$\frac{\partial}{\partial t}(\epsilon_L \rho_L) = -\frac{1}{A}\frac{\partial}{\partial x}(\epsilon_L \rho_L u_L A) + \frac{1}{A}\sum_k (\epsilon_L \rho_L v_L S_L)_k - (\Gamma_{LG} - \Gamma_{GL} + \dot{m}_{LG}) + \frac{S}{A}(m_D - m_E) + \frac{\partial}{\partial x}\left[\epsilon_L (D_{CL} + D_{CL}^T)\frac{\partial \rho_L}{\partial x}\right] - \frac{1}{A}\sum_k \left[S_L \epsilon_L (D_{CL} + D_{CL}^T)\frac{\partial \rho_L}{\partial L}\right]_k, \quad [A.3]$$

where

m_D = deposition rate of droplets
m_E = entrainment rate of droplets

and

S = wetted perimeter on A.

Energy equations

For the gaseous fluid,

$$\frac{\partial}{\partial t}(\epsilon_G \rho_G h_G) = -\frac{1}{A}\frac{\partial}{\partial x}(\epsilon_G \rho_G u_G A h_G) + \frac{1}{A}\sum_k (\epsilon_G \rho_G v_G S_L h_G)_k + (\Gamma_{LG} h_{Gs} - \Gamma_{GL} h_{Ls} + \dot{m}_{LG} h_{Gs}) + (\Gamma_{EG} h_{Gs} - \Gamma_{GE} h_{Ls} + \dot{m}_{EG} h_{Gs}) + \dot{q}_{IG} - \frac{\partial}{\partial x}(\epsilon_G q_{Gx}) + \frac{1}{A}\sum_k (S_L \epsilon_G q_{GL})_k + \ddot{Q}_{WG}, \quad [A.4]$$

where

h_G = specific enthalpy of the gas,
h_{Gs} = gas-saturated specific enthalpy,
h_{Ls} = liquid-saturated specific enthalpy,
$\dot{q}_{IG}$ = heat transfer rate to the gas from adjacent open sides,
q_{Gx} = thermal diffusion rate to the gas in the x-direction,
q_{GL} = thermal diffusion rate to the gas in the L-direction

and

$\ddot{Q}_{WG}$ = heat transfer rate to the gas from the wall.

Similarly, for the entrained liquid droplets,

$$\frac{\partial}{\partial t}(\epsilon_E \rho_E h_E) = -\frac{1}{A}\frac{\partial}{\partial x}(\epsilon_E \rho_E u_E A h_E) + \frac{1}{A}\sum_k (\epsilon_E \rho_E v_E S_L h_E)_k + (\Gamma_{GE} h_{Ls} - \Gamma_{EG} h_{Gs} - \dot{m}_{EG} h_{Gs}) - \frac{S}{A}(m_D h_E - m_E h_L) + \dot{q}_{IE} - \frac{\partial}{\partial x}(\epsilon_E q_{Ex}) + \frac{1}{A}\sum_k (S_L q_{EL})_k + \ddot{Q}_{WE}; \quad [A.5]$$

and for the liquid film,

$$\frac{\partial}{\partial t}(\epsilon_L \rho_L h_L) = -\frac{1}{A}\frac{\partial}{\partial x}(\epsilon_L \rho_L u_L A h_L) + \frac{1}{A}\sum_k (\epsilon_L \rho_L v_L S_L h_L)_k + (\Gamma_{GL} h_{Ls} - \Gamma_{LG} h_{Gs} - \dot{m}_{LG} h_{Gs})$$

$$+ \frac{S}{A}(m_D h_E - m_E h_L) + \bar{q}_{IL} - \frac{\partial}{\partial x}(\epsilon_L q_{Lx}) + \frac{1}{A}\sum_k (S_L \epsilon_L q_{LL})_k + \bar{Q}_{WL}. \quad [A.6]$$

Momentum equations

There are two equations for each fluid, in the x- and L-directions and referred to by subscripts x and L, respectively. For the gaseous fluid, the x-direction equations are

$$\frac{\partial}{\partial t}(\epsilon_G \rho_G u_G) = -\frac{\partial}{\partial x}(\epsilon_G \rho_G u_G^2) + \frac{1}{A}\sum_k (\epsilon_G \rho_G v_G u_G S_L)_k - \epsilon_G \frac{\partial P}{\partial x} - \epsilon_G \rho_G g_x - \bar{\tau}_{WGx} - \bar{\tau}_{LGx} - \bar{\tau}_{EGx}$$

$$+ (\Gamma_{LG} + \dot{m}_{LG})u_L - \Gamma_{GE} u_G + (\Gamma_{EG} + \dot{m}_{EG})u_E - \Gamma_{GE} u_G - \frac{\partial}{\partial x}(\epsilon_G \tau_{Gxx}) + \frac{1}{A}\sum_k (S_L \epsilon_G \tau_{GLx})_k, \quad [A.7]$$

where

P = pressure,
g_x = gravitational acceleration (in the x-direction),
$\bar{\tau}_{WGx}$ = wall to gas shear force per unit volume,
$\bar{\tau}_{LGx}$ = film to gas shear force per unit volume,
$\bar{\tau}_{EGx}$ = droplets to gas shear force per unit volume,
τ_{Gxx} = axial contribution of the axial molecular and turbulent viscous stress

and

τ_{GLx} = axial contribution of the lateral molecular and turbulent viscous stress.

The L-direction momentum equation for the gaseous fluid is

$$\frac{\partial}{\partial t}(\epsilon_G \rho_G v_G) = -\frac{\partial}{\partial x}(\epsilon_G \rho_G u_G v_G) - \frac{\partial}{\partial L}(\epsilon_G \rho_G v_G^2) - \epsilon_G \frac{\partial P}{\partial L} - \epsilon_G \rho_G g_L - \bar{\tau}_{WGL} - \bar{\tau}_{LGL} - \bar{\tau}_{EGL}$$

$$+ (\Gamma_{LG} + \dot{m}_{LG})v_L - \Gamma_{GL} v_G + (\Gamma_{EG} + \dot{m}_{EG})v_L - \Gamma_{GE} v_G$$

$$- \frac{\partial}{\partial L}(\epsilon_G \tau_{GLL}) - \frac{\partial}{\partial x}(\epsilon_G \tau_{GLx}). \quad [A.8]$$

The equations for the entrained droplets are

$$\frac{\partial}{\partial t}(\epsilon_E \rho_E u_E) = -\frac{\partial}{\partial x}(\epsilon_E \rho_E u_E^2) + \frac{1}{A}\sum_k (\epsilon_E \rho_E v_G u_G S_L)_k - \epsilon_E \frac{\partial P}{\partial x} - \epsilon_E \rho_E g_x - \bar{\tau}_{WEx} + \bar{\tau}_{EGx} + \bar{\tau}_{EFx}$$

$$- (\Gamma_{EG} + \dot{m}_{EG})u_E + \Gamma_{GE} u_G - \frac{S}{A}(m_D u_E - m_E u_L) \quad [A.9]$$

and

$$\frac{\partial}{\partial t}(\epsilon_E \rho_E v_E) = -\frac{\partial}{\partial x}(\epsilon_E \rho_E u_E v_E) - \frac{\partial}{\partial L}(\epsilon_E \rho_E v_E^2) - \epsilon_E \frac{\partial P}{\partial L} - \epsilon_E \rho_E g_L - \bar{\tau}_{WEL} + \bar{\tau}_{EGL} + \bar{\tau}_{ELL}$$

$$- (\Gamma_{EG} + \dot{m}_{EG})v_E + \Gamma_{GE} v_G - \frac{S}{A}(m_D v_E - m_E v_L). \quad [A.10]$$

The momentum equations for the liquid film are

$$\frac{\partial}{\partial t}(\epsilon_L \rho_L u_L) = -\frac{\partial}{\partial x}(\epsilon_L \rho_L u_L^2) + \frac{1}{A}\sum_k (\epsilon_L \rho_L v_L u_L S_L)_k - \epsilon_L \frac{\partial P}{\partial x} - \epsilon_L \rho_L g_x - \bar{\tau}_{WLx} + \bar{\tau}_{LGx} - \bar{\tau}_{ELx}$$

$$-(\Gamma_{LG} + \tilde{m}_{LG})u_L + \Gamma_{GL} u_G + \frac{S}{A}(m_D u_E - m_E u_L)$$

$$-\frac{\partial}{\partial x}(\epsilon_G \tau_{Lxx}) + \frac{1}{A}\sum_k (S_L \epsilon_E \tau_{LLx})_k \qquad [A.11]$$

and

$$\frac{\partial}{\partial t}(\epsilon_L \rho_L v_L) = -\frac{\partial}{\partial x}(\epsilon_L \rho_L v_L u_L) - \frac{\partial}{\partial L}(\epsilon_L \rho_L v_L^2) - \epsilon_L \frac{\partial P}{\partial L} - \epsilon_L \rho_L g_L - \bar{\tau}_{WLL} + \bar{\tau}_{LGL} - \bar{\tau}_{ELL}$$

$$-(\Gamma_{LG} + \tilde{m}_{LG})v_L + \Gamma_{GL} v_G + \frac{S}{A}(m_D v_E - m_E v_E) - \frac{\partial}{\partial L}(\epsilon_L \tau_{LLL}) - \frac{\partial}{\partial x}(\epsilon_L \tau_{LLx}). \qquad [A.12]$$

Combination equation

The mass conservation equations [A.1]–[A.3] may be summed to form a single combined mass conservation equation as follows:

$$\frac{\partial}{\partial x}(\epsilon_G \rho_G + \epsilon_E \rho_E + \epsilon_L \rho_L) = -\frac{1}{A}\frac{\partial}{\partial x}(\epsilon_G \rho_G u_G A + \epsilon_E \rho_E u_E A + \epsilon_L \rho_L u_L A)$$

$$+\frac{1}{A}\sum_k (\epsilon_G \rho_G v_G S_L + \epsilon_E \rho_E v_E S_L + \epsilon_L \rho_L v_L S_L)_k$$

$$+\frac{\partial}{\partial x}\left[\epsilon_G (D_{CG} + D_{CG}^T)\frac{\partial \rho_G}{\partial x}\right] + \frac{\partial}{\partial x}\left[\epsilon_E (D_{CE} + D_{CE}^T)\frac{\partial \rho_E}{\partial x}\right]$$

$$+\frac{\partial}{\partial x}\left[\epsilon_L (D_{CL} + D_{CL}^T)\frac{\partial \rho_L}{\partial x}\right] - \frac{1}{A}\sum_k \left[S_L \epsilon_G (D_{CG} + D_{CG}^T)\frac{\partial \rho_G}{\partial L}\right]_k$$

$$-\frac{1}{A}\sum_k \left[S_L \epsilon_E (D_{CE} + D_{CE}^T)\frac{\partial \rho_E}{\partial L}\right]_k - \frac{1}{A}\sum_k \left[S_L \epsilon_L (D_{CL} + D_{CL}^T)\frac{\partial \rho_L}{\partial L}\right]_k. \qquad [A.13]$$

Volume fraction equation

From the definition of the volume fractions,

$$\epsilon_G + \epsilon_E + \epsilon_L = 1. \qquad [A.14]$$

The set of 13 equations used are [A.1], [A.2], [A.13], [A.4]–[A.12] and [A.14].